Cycles of trace elements and isotopes in the ocean – GEOTRACES and beyond

Soluble iron conservation and colloidal iron dynamics in a hydrothermal plume[☆]

A.J.M. Lough[a,b,][*], W.B. Homoky[c], D.P. Connelly[b], S.A. Comer-Warner[a,1], K. Nakamura[d], M.K. Abyaneh[e], B. Kaulich[e], R.A. Mills[a]

[a] Ocean and Earth Science, National Oceanography Centre Southampton, University of Southampton, Southampton SO14 3ZH, UK
[b] National Oceanography Centre, European Way, Southampton SO14 3ZH, UK
[c] Department of Earth Sciences, University of Oxford, South Parks Road, Oxford OX1 3AN, UK
[d] National Institute of Advanced & Industrial Science & Technology, Tsukuba Central 7, 1-1-1 Higashi, Tsukuba, Ibaraki 3058567, Japan
[e] Diamond Light Source Ltd, Harwell Science & Innovation Campus, Didcot, Oxfordshire OX11 0DE, UK

ARTICLE INFO

ABSTRACT

Iron (Fe) limits or co-limits primary productivity and nitrogen fixation in large regions of the world's oceans, and the supply of Fe from hydrothermal vents to the deep ocean is now known to be extensive. However, the mechanisms that control the amount of hydrothermal Fe that is stabilized in the deep ocean, and thus dictate the impact of hydrothermal Fe sources on surface ocean biogeochemistry, are unclear. To learn more, we have examined the dispersion of total dissolvable Fe (TDFe), dissolved Fe (dFe) and soluble Fe (sFe) in the buoyant and non-buoyant hydrothermal plume above the Beebe vent field, Caribbean Sea. We have also characterized plume particles using electron microscopy and synchrotron based spectromicroscopy.

We show that the majority of dFe in the Beebe hydrothermal plume was present as colloidal Fe (cFe = dFe − sFe). During ascent of the buoyant plume, a significant fraction of particulate Fe (pFe = TDFe − dFe) was lost to settling and exchange with colloids. Conversely, the opposite was observed in the non-buoyant plume, where pFe concentrations increased during non-buoyant plume dilution, cFe concentrations decreased apparently due to colloid aggregation. Elemental mapping of carbon, oxygen and iron in plume particles reveals their close association and indicates that exchanges of Fe between colloids and particles must include transformations of organic carbon and Fe oxyhydroxide minerals. Notably, sFe is largely conserved during plume dilution, and this is likely to be due to stabilization by organic ligands, in contrast to the more dynamic exchanges between pFe and cFe.

This study highlights that the size of the sFe stabilizing ligand pool, and the rate of iron-rich colloid aggregation will control the amount and physico-chemical composition of dFe supplied to the ocean interior from hydrothermal systems. Both the ligand pool, and the rate of cFe aggregation in hydrothermal plumes remain uncertain and determining these are important intermediate goals to more accurately assess the impact of hydrothermalism on the ocean's carbon cycle.

This article is part of a special issue entitled: "Cycles of trace elements and isotopes in the ocean – GEOTRACES and beyond" - edited by Tim M. Conway, Tristan Horner, Yves Plancherel, and Aridane G. González.

1. Introduction

Hydrothermal fluids are enriched in iron (Fe) and manganese (Mn) relative to seawater (German and Von Damm, 2004; Von Damm et al., 1985) and provide a potentially important source of these biologically essential metals for ocean primary production (Martin, 1990). Understanding processes that control the exchange of Fe between the soluble ($< 0.02\,\mu m$), colloidal (0.02 to $0.2\,\mu m$) and particulate ($> 0.2\,\mu m$) size fractions is especially critical for establishing the impact of hydrothermal plumes on the inventory of Fe and potentially other trace

---

elements in the deep ocean. There is limited information from hydrothermal plumes on the partitioning of Fe between the soluble, colloidal and particulate fractions because most studies have focused on plume particles (Bertram et al., 2002; Breier et al., 2012; Cowen et al., 2001; Edmonds and German, 2004; Feely et al., 1996, 1994b, 1998; German et al., 1991; Klevenz et al., 2011; Revels et al., 2015; Toner et al., 2009a, 2009b).

Early studies examining hydrothermal plume particles found H_2S concentration is a major control on Fe mineralization. Fe precipitated as metal sulphides, such as pyrite (FeS_2), pyrrhotite ($Fe_{(1-x)}S$) and chalcopyrite ($CuFeS_2$), where elevated H_2S concentrations persisted (Edmonds and German, 2004; Feely et al., 1994a; German et al., 1991). However, where H_2S is depleted, Fe mineral formation is dominated by the oxidation of reduced Fe(II) to Fe(III), forming Fe oxyhydroxides. Subsequent oxidative dissolution of particulate metal sulphides in oxygenated seawater may transfer Fe back to the dissolved size-fraction over longer periods of time (Feely et al., 1987; German et al., 1991; Klevenz et al., 2011; Metz and John, 1993; Revels et al., 2015). Recent work using *in situ* filtration indicates these early studies may have overestimated the extent of Fe sulphide precipitation in plumes (Waeles et al., 2017) and hence the role of this process in determining plume-derived Fe fluxes may be less significant than previously thought.

Dissolved Mn has much slower oxidation-reaction rates than Fe in the ocean and is therefore more readily conserved in hydrothermal plumes (Breier et al., 2012; Feely et al., 1994b; Resing et al., 2015). Whilst there is evidence of dissolved Mn being scavenged by bacteria, and for Mn sulphide precipitation in hydrothermal plumes (Breier et al., 2012; Cowen et al., 1986), these losses represent only a minor fraction of vent derived Mn (Cowen et al., 1990; Findlay et al., 2015; James and Elderfield, 1996). Thus, the quasi-conservative nature of dissolved Mn provides as a powerful tracer of hydrothermal plume dilution near ocean spreading centres.

The longevity of Fe in hydrothermal plumes and the distribution of Fe between different size fractions varies across ocean basins, with anywhere from 0 to 96% of dissolved Fe (dFe; $< 0.2\,\mu m$) present as colloids (Fitzsimmons et al., 2014, 2015b; Hawkes et al., 2013; Nishioka et al., 2013). Despite soluble Fe (sFe; $< 0.02\,\mu m$) comprising only a fraction of dFe concentrations measured in hydrothermal plumes, sFe within plumes is still higher than background seawater sFe concentrations (Fitzsimmons et al., 2014, 2015b; Hawkes et al., 2013; Nishioka et al., 2013). Due to very slow nano-particulate settling rates, and the stabilizing effects of organic ligands, the colloidal and soluble species of Fe in hydrothermal plumes may persist in the oceans much longer than predicted by Fe(II) oxidation rates or Fe(III) solubility alone (Hawkes et al., 2013; Kleint et al., 2016; Yucel et al., 2011). The long-range dispersal of hydrothermal plumes also appears to be supported by continuous exchange of Fe between the dissolved and particulate fractions (Fitzsimmons et al., 2017a; Homoky, 2017). Thus, there is mechanistic evidence that an important fraction of vent sourced dFe may be transported to regions of upwelling and impact the surface ocean (Tagliabue et al., 2010). Critically, what remains to be learned is precisely how, and how much of this dFe may be supplied from hydrothermal vents to the deep ocean.

The speciation of cFe and sFe and the processes by which Fe is exchanged between these fractions and the particulate fraction (pFe) is largely unknown, both in hydrothermal plumes, and more widely in the open ocean. At least three different species of dFe have been identified in different stages of hydrothermal plumes, which could explain the occurrence of elevated levels of cFe and/or sFe. Colloidal-sized pyrite has been measured in vent fluids (Findlay et al., 2015; Gartman et al., 2014; Yucel et al., 2011) but not in plumes. Dissolved Fe, stabilized by complexation with organic ligands, has been observed in plumes, which may slow both the process of Fe(II) oxidation and the subsequent formation of Fe oxyhydroxide particles (Bennett et al., 2008; Hawkes et al., 2013; Sander and Koschinsky, 2011; Statham et al., 2005). Many studies have confirmed the prevalence of Fe oxyhydroxide particles in

plumes (Breier et al., 2012; Fitzsimmons et al., 2017a; Hoffman et al., 2018; Klevenz et al., 2011; Sands et al., 2012). Recent work using Fe isotopes indicates that a fraction of hydrothermal cFe may be Fe oxyhydroxides (Fitzsimmons et al., 2017a), however, this relies on assumptions about the isotopic composition of colloidal Fe oxyhydroxides and there is no method currently available for directly measuring colloidal Fe oxyhydroxide in plumes.

In all likelihood, the hydrothermal dFe pool may be a combination of the different Fe species discussed above. With the premise that most of the inorganic mineral colloids will be $> 0.02\,\mu m$ in size and therefore present in the colloidal fraction, Fe organic complexes will be present across both soluble and colloidal size fractions and aqueous Fe will only be present in the soluble fraction. Herein we seek to understand the processes controlling the partitioning of Fe amongst the operationally defined soluble, colloidal and particulate fractions and aim to quantify the exchanges of Fe between them during hydrothermal plume dilution with seawater so we may assess their impact on the supply of dFe to the deep ocean.

Our experimental approach uses a combination of microscopy and bulk chemistry techniques from samples taken within 1.2 km of a hydrothermal vent site on an ultraslow spreading ridge. Fe concentration measurements reveal how Fe is transferred between our operationally defined size fractions and microscopy results give further insight into the composition and oxidation state of Fe in particulates, helping us to understand what processes are causing the transfer of Fe amongst these size fractions. The scale of our sampling captures the rarely studied transition between the localized studies of vent fluids and the basin scale studies of GEOTRACES. Moreover, we present results from an ultra-slow spreading ridge which are relatively unexplored for venting globally and are assumed to have a less significant impact on the ocean iron inventory in comparison to fast spreading ridges (Resing et al., 2015; Tagliabue et al., 2010).

2. Materials and methods

2.1. Geological setting

Plumes and vents associated with ultra-slow spreading ridges ($< 20\,mm\,yr^{-1}$) are under sampled globally compared to other ridge axes and have been identified as key sites to further constrain the hydrothermal Fe flux (German, 2016). Furthermore, as they are underrepresented in models where Fe flux is a function of ridge spreading rate (Saito et al., 2013; Tagliabue et al., 2010), understanding the Fe chemistry of these plumes is key to improving current models. Samples were collected from a plume over the Beebe Vent Field (BVF), located on the ultra-slow spreading ($15\,mm\,y^{-1}$) Mid-Cayman Spreading Center (MCSC). The Cayman Trough is located in the Caribbean Sea south of the Cayman Islands (Fig. 1).
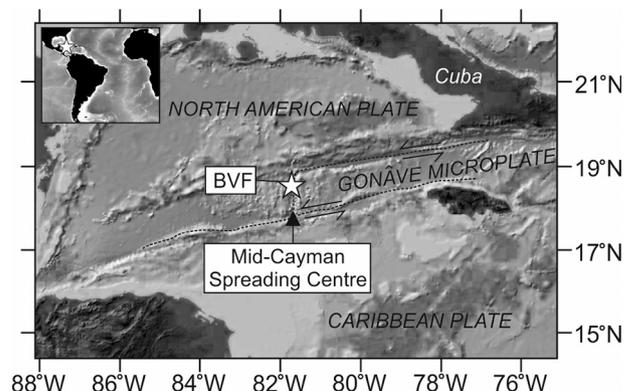

Fig. 1. Location of Mid-Cayman spreading centre (MCSC) (inset) and bathymetry map of the Mid Cayman Rise.

The BVF is located close to the axis of the MCSC and consists of six discrete metal sulphide mounds with active and inactive black smoker chimneys and areas of diffuse flow. Areas of active venting are associated with the three southernmost largest mounds, which are ~60 m wide.

The BVF is located at 18°32′47.7 N 81°43′05.5 W and 4960 m depth, making it the deepest hydrothermal vent field discovered to date (Connelly et al., 2012). There are three sites of active, black smoker-type venting. Beebe Woods is located to the south of the site at a depth of 4956 m (Fig. 1). Beebe 125 and Deepest Vents are located on a separate mound 50 m to the north of Beebe Woods, at depths of 4957 and 4964 m, respectively. The temperature and pH of fluids emanating from Deepest Vents and Beebe 125 are similar, 393 to 401 °C and 3.9 to 2.9 respectively. The temperature of fluids emanating from Beebe Woods is lower, 354 °C, with a higher pH range of 3.5 to 4.8. Hydrothermal fluids circulate through mafic and ultramafic lithologies beneath the BVF (Webber et al., 2015). As a result of the high temperature venting at this site previous studies have recorded a buoyant plume that rises ~1100 m reaching neutral buoyancy with the surrounding seawater at a height of ~4000 m which is in contrast with other vents where plumes rise 200 to 400 m (Connelly et al., 2012).

Previously, some works have also referred to the BVF as "Piccard" after the discovery of hydrothermal plume signals in the water column (German et al., 2010). In this study we refer to the Beebe Vent Field as it has been named in the InterRidge database, following its discovery at the seafloor (Beaulieu et al., 2013; Connelly et al., 2012).

Hydrographically the deep water in the Cayman Trough has temperature, salinity and O_2 concentration consistent with altered North Atlantic Deep Water (NADW) (Connelly et al., 2012) (Supplementary information, Table S1). Therefore, the vent fluids mix with deep waters with an oxygen concentration similar to the N. Atlantic and we calculate an oxidation half-life for Fe(II) of 0.28 h at this site based on the nearest available data (Table S.1) which is similar to those of plumes over the Mid-Atlantic Ridge (MAR). It is likely that this altered NADW enters the Cayman basin *via* the Oriente Fracture Zone from the Windward Passage (Johns et al., 2002). However, there is presently little data available on the chemistry and movement of deep water masses in the Cayman Trough and the Caribbean Sea.

2.2. Sampling and analysis of hydrothermal vent fluids

Gas tight samplers (IFREMER, Brest, FR) were used to sample high temperature vent fluids with temperatures measured separately within the orifice of chimneys using a probe deployed by the remotely operated vehicle (ROV) *Isis*. Getting vent fluid samples from the orifice of chimneys without any of the chimney material breaking away proved to be very difficult due to the narrow fragile structure. This meant there was an increased probability that small chimney fragments were sucked up by the sampler and partially dissolved before the sample could be recovered and filtered on deck. This is considered carefully when assessing the vent fluid results.

The vent fluid was diluted 100 fold in 0.3 M sub-boiled (S.B.) HNO_3 spiked with 20 ppb Be, 5 ppb In, and 5 ppb Re as internal standards. Diluted vent fluids were analysed by ICP-MS (X-series, *Thermo Scientific*) for Cu concentrations and ICP-AES (iCAP 6000, *Thermo Scientific*) for Fe, Mn and Magnesium (Mg). Instrument performance determined the method blank and error. All concentrations measured were sufficiently higher than the instrument limit of detection (l.o.d) and blank to avoid baseline interferences. The error was quantified by the relative standard deviation (RSD %) of instrument analysis, which was 2% for Fe, 2% Cu, 2% for Mg and 1% for Mn. H_2S was determined by iodimetric titration with 0.1 M $Na_2S_2O_3$ (± 2%).

## 2.3. Sampling of the hydrothermal plume waters and particles

Samples were collected from the RRS *James Cook* (voyage JC82,

February 2013). Detection and sampling of the hydrothermal plume was conducted using a *Seabird* 911+ conductivity, temperature and depth (CTD) profiler system attached to a titanium frame, which holds 24 externally sprung 10 L OTE (*Ocean Test Equipment*) water sampling bottles and a Stand Alone Pumping System (SAPS) for the collection of particles from large volumes of seawater. OTE bottles were cleaned at the start of each cruise by filling each bottle with freshwater and ~1 L of 20% HCl. The OTE bottles were Teflon lined with Teflon taps and non-metallic parts to prevent any contamination during sampling of waters with low concentrations of trace metals. A light scattering sensor (LSS) and Eh electrodes were also mounted on the base of the titanium rosette frame.

Non-buoyant plume particles were collected by *in situ* filtration of 1060 L of seawater at 4089 m depth using the SAPS. Immediately after recovery filter (1 μm pore size, *Whatman*, 293 mm) surfaces were rinsed with sufficient de-ionised water (Milli-Q, Millipore, > 18.2 mΩ cm^{-1}) to cover the surface of the filter, which was subsequently pulled through the filter by vacuum pump. This was repeated several times to prevent salt crystallisation on the filter. SAPS filters were frozen and stored at −20 °C. The process of collecting the SAPS filters on deck took ~15 min and was done as quickly as possible in order to limit the exposure of particles to ambient atmosphere and minimise any oxidation of residual Fe^{2+} or fine grained Fe-sulphides. However, it is important to note that the SAPS filter was in oxygenated seawater for 4 h during sample collection and the Fe oxidation half-life for seawater in the Cayman trench is 0.28 h (Supplementary information, Table S.1). Theoretically this should be enough time to oxidise the majority of any residual Fe (II) if the concentration in the plume is in the 100's of nM range. This means that any Fe (II) present in these particulate samples is therefore likely to be a relatively stable and persistent form of Fe (II) in the water column.

Hydrothermal plumes were located using the CTD profiler, LSS and Eh electrodes to identify deviations in temperature, light scattering, and Eh from background seawater (Figs. 3 and S1). We refer to Eh in this work as the measurement of voltage of the inert (Pt) electrode against the reference Ag-AgCl electrode in saturated KCl solution, and not in the strict sense of the physical chemistry definition of Eh. The buoyant part of the hydrothermal plume was identified by negative Eh anomalies and positive temperature and LSS anomalies. The non-buoyant plume was detected by positive particle anomalies, there were no changes in salinity and temperature associated with the non-buoyant plume as a result of deep water entrainment. This is most likely the result of the homogeneity of temperature and salinity within the Cayman basin at depth. The direction of non-buoyant plume dispersal is controlled by ambient deep water currents, which at the time of sampling transported the plume in a north northwest direction.

Sampling depths ranged from 3911 to 4952 m with all samples collected within 1.2 km distance of the vent field (Fig. S1). These samples spanned the depth-range of buoyant plume and non-buoyant plume signals, which were observed previously and during this study (Bennett et al., 2013; Connelly et al., 2012; German et al., 2010) Samples were filtered on deck as soon as possible to mitigate any in bottle effects (within ~4 h of the niskin bottle closing in the water column) (Fig. S.3). Prior to the collection of every seawater sample, trace metal clean LDPE sample bottles were emptied, rinsed with deionised water, and then pre-conditioned by rinsing with an aliquot of the sample water and discarding it to waste. Unfiltered seawater was collected for its total dissolvable (TD) Fe and Mn. Polycarbonate membrane filters (0.2 μm pore size, 47 mm diameter, *Whatman*) were connected to OTE bottles using Teflon filter housings to filter 125 mL seawater for dissolved trace metals (dFe and dMn). A separate 125 ml LDPE bottle was filled with unfiltered sample water for separating the soluble fraction. Unfiltered water was passed through a 0.2 μm cellulose acetate syringe filter (*Whatman*) and a 0.02 μm aluminium oxide syringe filter (Anotop; *Whatman*) connected in series, at a rate of 1 ml min^{-1} using a peristaltic pump and polyvinyl chloride tubing
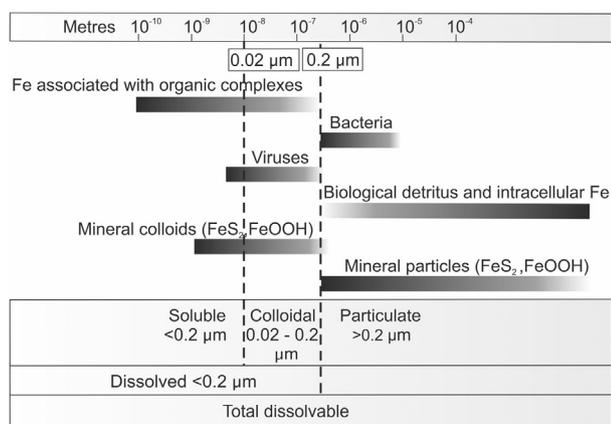
Fig. 2. Different chemical species discussed in this paper that add to the concentration of trace metals in different size fractions. This is not intended to be a comprehensive list of all Fe species present in these size fractions, only the ones considered to have a major influence on plume Fe content. The pore sizes of filters used are shown by dashed lines. Total dissolvable is defined as anything that dissolves in an unfiltered sample after being acidified with HNO_3 to a pH of 1.7 to 1.8 for > 1 year. The colloidal fraction is derived as the difference between soluble and dissolved. The particulate fraction is derived from the difference between dissolved and total dissolvable.
Adapted from Aiken et al. (2011).

(*Elkay*). The connected filtration set-up was rinsed through with 40 ml 0.015 M ultra-pure HCl (*ROMIL* UpA) followed by a 4 h circulation of 200 ml of deionised water prior to use. The first 20 ml of sample water passed through the soluble filtration system was used to rinse a sample bottle and then discarded. A final minimum of 40 ml was then collected for soluble Fe (sFe) (Wu et al., 2001). All water samples for Fe and Mn analysis were acidified (pH 1.7 to 1.8) using ultra-pure HNO_3 (*ROMIL* UpA) and analysed after > 1 year.

Unfiltered seawater and seawater filtered through 0.2 and 0.02 μm membranes were used to provide operational distinctions between TDFe, particulate Fe (pFe; > 0.2 μm), dFe (< 0.2 μm), colloidal Fe (cFe; > 0.02 < 0.2 μm), and sFe (< 0.02 μm). Where TDFe, dFe and sFe are measured values, and pFe and cFe are derived as; pFe = TDFe − dFe and cFe = dFe − sFe (Fig. 2). The calculated concentrations of pFe and cFe are assumed to be below the l.o.d. if they are less than the propagated analytical error of measured values. These operational distinctions are frequently used by the marine science community (Aquilina et al., 2014; Boye et al., 2010; Cullen et al., 2006; Fitzsimmons et al., 2014, 2015b; Hawkes et al., 2013; Homoky et al., 2011; Nishioka et al., 2013) as defined in Fig. 2. They are not directly comparable to the chemical definition of a colloid as particles in the range of 0.001 to 10 μm with linear dimensions (Berg, 2010; Russel et al., 1989) or the definition of a nanoparticle as a particle in the range of 1 to 100 nm where atomic properties make the transition to mirco or macroscopic properties (Israelachvili, 2011).

2.4. Determination of Fe and Mn in hydrothermal plume samples

Trace metal concentrations in samples were measured by pre-concentration of 15 ml sub-sampled aliquots onto a chelating resin (Kagaya et al., 2009). Samples were processed using an offline extraction system similar to that used by Milne et al. (2010) but using the standard addition procedure developed by Biller and Bruland (2012). The 1 M S.B. HNO_3 eluent from this process was measured using an Element XR (Thermo scientific) (Biller and Bruland, 2012; Milne et al., 2010). Drift corrections were applied to data using standard bracketing by measuring a standard solution of intermediate concentration every 10 samples.

The methodological blank for Fe and Mn was 0.08 and

0.004 nmol kg^{-1} respectively with a detection limit of 0.09 and 0.003 nmol kg^{-1} (3σ of blank $n = 12$). The certified reference material NASS-6 (*National Research Council Canada*) was taken through the same extraction procedure as a check on the recovery of trace metals and reproducibility of the method. Measured concentrations of NASS-6 for Fe and Mn were 9.1 ± 0.7 and 8.7 ± 0.6 nmol kg^{-1} ($n = 6$) compared to certified values of 8.65 ± 0.81 and 9.39 ± 0.86 nmol kg^{-1}.

2.5. Mineralogical composition of plume particles by SEM-EDX and synchrotron techniques

Particulates from the non-buoyant plume collected on SAPS filters were analysed for size and elemental composition to assess the chemistry of particles that are transported away from the vent field. In order to concentrate the particles from the SAPS filter onto a smaller area for microscopy the SAPS filter was rinsed with de-ionised water which was then filtered through acid washed polycarbonate filters (*Whatman*, 0.2 μm pore size, 47 mm diameter).

Sections were cut from the polycarbonate filter using ceramic scissors rinsed prior to use with deionised water, the remainder of the filter was stored frozen at −20 °C for spectromicroscopy analysis at a later date. Cut filter sections were mounted onto metal stubs with carbon tape for analysis using the scanning electron microscope (SEM) (Carlseiz LEO 1450VP). Particle morphology and composition were examined using the backscatter detector on the SEM, and elemental composition of particles was determined using an energy dispersive X-ray (EDX) detector (Princeton Gamma Technology Light Element Detector), built-in to the SEM. In order to get results that are representative of the abundance of metal rich particles in the NBP the filter surface was examined in a grid pattern as described in Lough et al. (2017). These results are presented in full in Table S2.

The mineralogy of particles was determined using the relative atomic percent of elements. Fe bearing particles with no sulphur peaks on EDX spectra were assumed to be Fe oxyhydroxides. The precise mineralogy of these particles cannot be determined by EDX analysis due to poor sensitivity associated with low atomic weight elements such as oxygen (Goldstein et al., 2003). Due to the short time scales of plume dilution the formation of more crystalline Fe oxides such as hematite or goethite is unlikely to have occurred and Fe oxyhydroxides have been shown to be the prevailing Fe-oxide phase in previous plume studies (Breier et al., 2012; Fitzsimmons et al., 2017a; Hoffman et al., 2018; Toner et al., 2009a).

To determine the Fe oxidation state and likely mineralogy of Fe-rich particles that could not be determined by SEM-EDX, particles were examined using the scanning transmission X-ray microscope (STXM - I08 beamline) at the Diamond Light Source synchrotron (UK). Particles were mounted onto supports in a positive flow glove box continuously flushed with N_2 in order to limit exposure of samples to ambient atmosphere. Filter segments were defrosted and suspended in de-ionised water (equilibrated with the N_2 enriched atmosphere of the glove box) in a centrifuge tube, this was then shaken to release particles from the surface of the filter. Particles suspended in solution were mounted on standard (3 mm) square mesh grids (*Agar Scientific*) or silicon nitride membranes (2.65 mm) (*Silson*). Grids and membranes were glow discharged prior to loading the sample in order to improve particle distribution across the surface of the sample support. Between 2 and 10 μL of particle suspension was pipetted onto membranes and left to dry in the glove box. The sample support was loaded into the I08 customised holder, which was placed into the microscope.

Both the X-ray absorption near edge structure (XANES) and X-ray fluorescence (XRF) of particles was analysed which covers the 280 to 4400 eV photon energy range. XANES were conducted at the Fe *L*-edge (700 to 730 eV) to examine oxidation state of Fe within particles. Photon energy was calibrated using N_2 gas spectra to measure the photon flux. X-ray absorption stacks were processed using the software MANTiS (Lerotic et al., 2014), which was used to align images,

normalized using I_0 (incident X-ray beam without sample), subtract dark (background signal without X-ray beam) and fit peaks to spectra. The near-edge peak splitting seen in Fe *L*-edge absorption spectra is indicative of the oxidation state of Fe (Fitzsimmons et al., 2017a; Hoffman et al., 2018; Toner et al., 2009a; von der Heyden et al., 2012). The intensity of the initial near-edge peak is representative of Fe(II) and the intensity of the preceding peak representative of Fe(III) abundance (de Groot, 2009). Measured spectra were calibrated to the apex of the known energy peak for Fe (III) from published standard spectra of 709.5 eV (Fitzsimmons et al., 2017b; Hawkings et al., 2014; Hoffman et al., 2018; Toner et al., 2009a; von der Heyden et al., 2012). Iron rich regions are classified as either pure Fe(III), Fe(III) rich mixed valence, Fe(II) rich mixed valence or pure Fe(II) based on the intensity of the near edge and proceeding peak as described in von der Heyden et al. (2012). Pyrrhotite and pyrite standard spectra show no splitting of the near-edge peak compared to Fe oxides (Toner et al., 2009a). No sample regions were comparable to published spectra for pyrite or pyrrhotite however, this is because our analysis was focused on examining regions where Fe was located with C and O and not S. This is because pyrite had already been identified by SEM-EDX and the focus of the synchrotron analysis was to examine Fe(II)-Fe(III)-C relationships in particles.

The I08 beamline implements a large-area, single element SDD detector optimized in backscatter configuration for X-ray fluorescence detection down to an atomic weight of carbon. Synchrotron XRF data were calibrated in PyMCA and used to assess the distribution of Fe relative to C and O. This is useful for determining whether or not significant amounts of particulate Fe are associated with C (Fitzsimmons et al., 2017a; Toner et al., 2009a, 2016). It is assumed that C detected is organic C and there is little to no carbonate minerals in particulate samples, which is reasonable given that hydrothermal plumes are typically depleted in particulate inorganic carbon and enriched in particulate organic carbon compared to background seawater (Bennett et al., 2011; Hoffman et al., 2018; Lam et al., 2017).

3. Results

The strongest Eh and temperature signals over BVF coincided at a maximum depth of ~4870 m, indicative of the early buoyant plume (Fig. 3). These anomalies were persistent up to a minimum depth of ~4480 m, and likely reflect rising waters from multiple vents clustered closely together on the seafloor combined with entrainment of ambient deep water. Below ~3000 m ambient water temperature increases with depth due to adiabatic heating and temperature anomalies from the plume are superimposed on this increase. The temperature anomalies we measured are deeper than the extent of previous temperature anomalies, which were reported up to ~4000 m (Connelly et al., 2012; German et al., 2010). There were no temperature anomalies associated with the non-buoyant plume from entrainment of deep waters (Fig. S2). We detected particle anomalies between 4080 and 4480 m depth,

which we interpret to be particle dense layers of the buoyant plume. The non-buoyant plume was characterized by a higher density of particle anomalies between 4000 and 4080 m depth (Figs. 3 and S1).

3.1. Hydrothermal vent fluid end-member Fe and Mn

Magnesium is depleted in vent fluids relative to seawater as a result of hydrothermal circulation and behaves conservatively during venting and seawater mixing (Bischoff and Dickson, 1975; Bischoff and Seyfried, 1978). Therefore, Mg is used to estimate the purity of hydrothermal end members (Fig. 4) (Douville et al., 2002; Edmond et al., 1979; Israelachvili, 2011; James et al., 1995; James et al., 2014; Vondamm and Bischoff, 1987). Using this criterion, the concentration of Fe in the hydrothermal end member at BVF was 6.79 mmol kg^{-1} Fe and 0.62 mmol kg^{-1} for Mn. Several vent fluid samples were excluded from the Fe end member estimate as high Cu concentrations suggest dissolution of chimney material (which is 47 wt% Cu (Webber et al., 2015)) within the sample resulted in additional Fe in the fluid (Fig. 4).

Hydrogen sulphide in BVF samples ranged from 0.26 to 6.7 mmol kg^{-1}, but end member H_2S concentrations cannot be calculated in the same way as for Fe, because H_2S has no linear correlation with Mg. The average Fe/H_2S ratio of the Beebe 125 vent fluid samples is 1.6 showing Fe is in excess of H_2S in vent fluids, similar to other ultramafic hosted vent sites such as Rainbow on the MAR (Douville et al., 2002).

### 3.2. TDFe budget during hydrothermal plume-seawater mixing

Throughout this study dMn is used as a tracer of plume-seawater mixing due to the high concentrations present in the vent fluid (615 µmol kg^{-1}) compared to background seawater (0.1 nmol kg^{-1}). Similar to Fe, Mn is in the reduced form in the hydrothermal vent fluids and is continually oxidised by exposure to oxygenated seawater during plume dispersion. Unlike Fe, the oxidation of dMn occurs on time scales of days to weeks (rather than minutes to hours in the case of Fe) (Cowen et al., 1990) and given the scale of our sampling within 1.2 km of the vent source it is unlikely that enough Mn oxidation has occurred that would inhibit our use of dMn as a tracer of the plume. Repeat sampling from the same niskin bottle over time showed no change in the dMn concentration over the course of 16 h (Fig. S3).

Several processes are able to change the TDFe concentrations within a hydrothermal plume. For a metal such as Fe that is highly enriched in the hydrothermal fluid relative to seawater, dilution during plume-seawater mixing will rapidly lower the concentration of TDFe as the plume is dispersed (Field and Sherrell, 2000; James and Elderfield, 1996). An excess of TDFe compared to estimated TDFe from dMn dilution could also occur by entraining dMn poor Fe-rich waters into the plume or non-conservative behavior of dMn relative to TDFe.

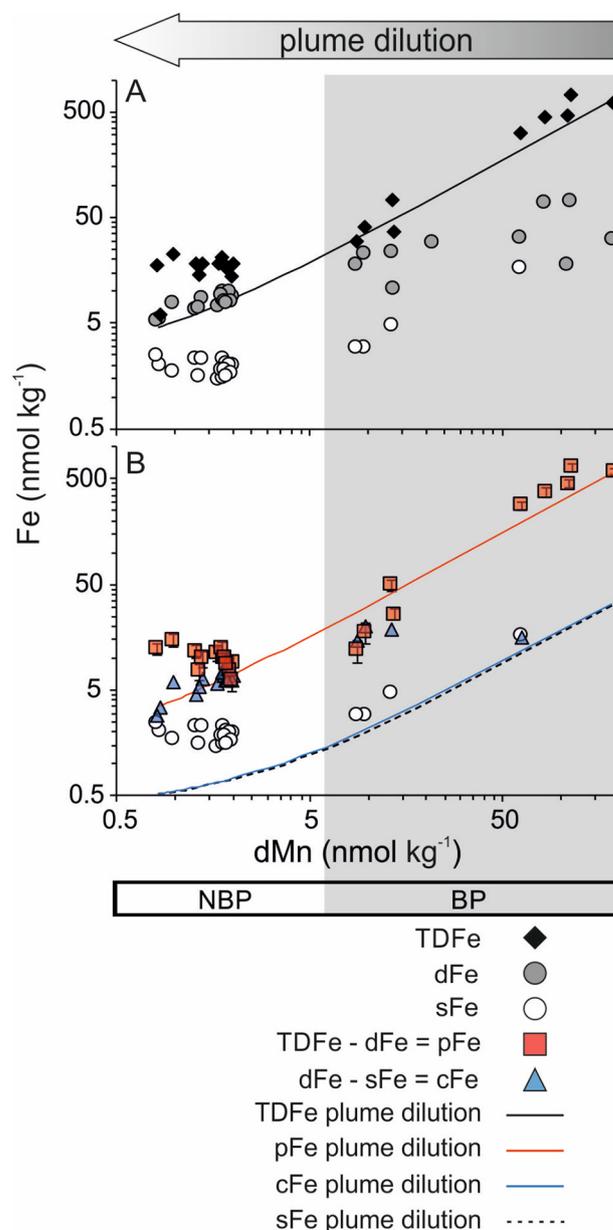Concentrations of TDFe in the BVF plume ranged from 6 to
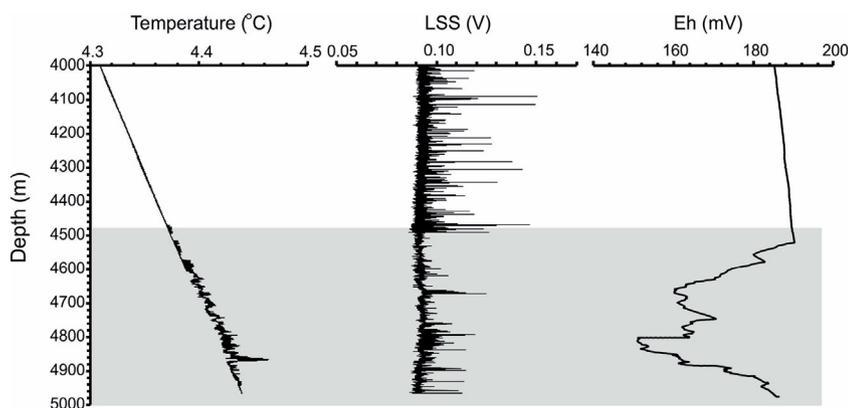
Fig. 3. The detection of hydrothermal plume anomalies in the water column over the BVF for temperature, Eh and light scattering (LSS). Grey shaded areas indicate the buoyant plume depths. Particle anomalies at depths shallower than 4480 are attributed to the non-buoyant plume. All sensor data is available from the British Oceanographic Data Centre (BODC) (https://www.bodc.ac.uk/).
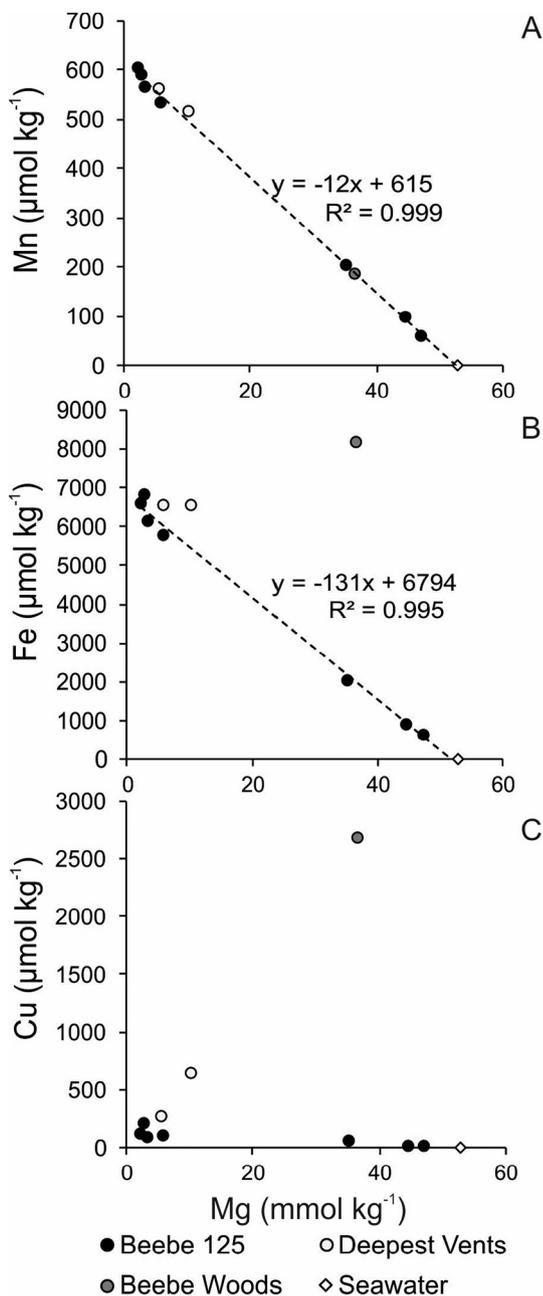
Fig. 4. Concentrations of Mn (A) Fe (B) and Cu (C) and Mg in hydrothermal vent fluid samples (circles) from BVF black smoker vents. Seawater by comparison (white diamond) has higher Mg and much lower Fe concentration. The dashed line shows linear regression used to extrapolate the end member vent fluid concentration. The regression includes all samples from Beebe 125 (black circles). Samples from Deepest Vents (light grey) and Beebe Woods (dark grey) are excluded from the regression based on high Cu concentrations. This indicates these samples had additional Fe added from the dissolution of chalcopyrite ($CuFeS_2$) that broke off from the friable chimneys during sampling and therefore are not representative of Fe concentrations in the vent fluid.

Fig. 5. Measured TDFe (black diamond), dFe (grey circle) and sFe (white circle) concentrations relative to dMn in the BVF hydrothermal plume (A). The TDFe and dFe fractions can be further separated into pFe (red squares) and cFe (blue triangles) (B), error bars are only shown where they are larger than the symbol size. The arrow indicates plume mixing with seawater and concentrations of dMn decrease by dilution. The solid line in panel A is the estimated TDFe concentration from conservative dilution of the highest concentration plume sample, likewise in panel B dashed lines represent predicted conservative dilution of sFe (black small dash), cFe (blue line) and pFe (red line). Conservative mixing is calculated using Eq. (S1) (Supplementary information). The grey background and bar underneath the x-axis indicate which samples were taken from depths corresponding to the buoyant plume and non-buoyant plume as shown in Fig. 3.

712 nmol kg^{-1} and decreased with dMn which ranged from 0.8 to 189 nmol kg^{-1} (Fig. 5). The sample with the highest dMn concentration is the most proximal to the vent source at the seafloor however, it is likely that there is a spatial gap in our sampling between the vent fluid samples taken directly from the vent orifice and the rosette over the vents. The most proximal plume sample has a TDFe/dMn ratio of 3.3 compared to the vent fluid Fe/Mn of 11.0. Assuming dMn behaves conservatively this equates to a loss of 70 ± 8% of the Fe from the vent fluid in the very early stages of the buoyant plume that wasn't sampled

between the rosette and the ROV. This Fe loss is inconsistent with average TDFe/dMn ratio of the non-buoyant plume which is similar to the end member vent fluid value of 11.8 (*n* = 16) and suggests the majority of Fe from the vent fluid is transferred to non-buoyant plume height. The concentration of TDFe was equal to that predicted from dilution of the most vent proximal plume sample (Supplementary information, Eq. (S1)) during dispersion of the buoyant plume (Fig. 5). The majority of TDFe samples lie above the conservative mixing line in

the non-buoyant plume which shows an excess of Fe relative to what would be predicted from calculating the dilution of buoyant plume TDFe using dMn (Figs. 5 and S1).

3.3. Size fractionation of Fe during hydrothermal plume-seawater mixing

TDFe of plume samples contained on average $64 \pm 18\%$ pFe with $35 \pm 13\%$ in the cFe fraction and $11 \pm 6\%$ as sFe. The highest concentrations of sFe and dFe were 16 and 71 $nmol\,kg^{-1}$, respectively, which decreased to observed minima of 1 and 5 $nmol\,kg^{-1}$ in the non-buoyant plume. When considering the balance between sFe and cFe within the dissolved fraction, as the buoyant plume became progressively diluted cFe increased from 49 to 87% of dFe and sFe decreases from 51 to 13% of dFe. This trend was reversed in the non-buoyant plume where cFe decreases from 82 to 54% of dFe and sFe increases as a fraction of dFe but only as a result of losses in cFe as the concentration of sFe does not vary ($1.9 \pm 0.3\,nmol\,kg^{-1}$ ($n = 16$)). A notable exception to this trend was in the shallowest sample (*i.e.* lowest dMn content), where each of these fractions was a larger proportion (33 and 58% respectively) of TDFe.

The relationship between Fe fractions and dMn contents in the plume is described by comparison to conservative dilution of the most proximal plume sample (mentioned in Section 3.2) with N. Atlantic seawater, assuming that separation of Fe into sFe, cFe and pFe in the initial stages of mixing is the same as the most proximal plume sample with the least seawater dilution where we have samples for sFe, dFe and TDFe (Fig. 5B and Table S4). Whilst sFe lies above the conservative mixing line the data points run parallel to the mixing line in the buoyant plume, which is indicative of quasi-conservative behavior similar to dMn. The pFe concentrations also run parallel to the conservative mixing line in the buoyant plume with the exception of 3 samples in the most dilute part of the buoyant plume (Fig. 5B) which may indicate loss of pFe relative to dMn. In the non-buoyant plume pFe began to increase relative to dMn with concentrations greater than the conservative mixing line (Fig. 5B). Likewise, sFe concentrations were elevated relative to conservative mixing in the non-buoyant plume and appear to be maintained at a baseline level of $1.9 \pm 0.3\,nmol\,kg^{-1}$ ($n = 16$). Colloidal Fe in the buoyant plume is greater than the conservative mixing line, which indicates a net addition of cFe relative to dMn. In the non-buoyant plume, cFe decreased relative to dMn. Therefore, to a first approximation, the changes in cFe oppose the changes in pFe during buoyant plume and non-buoyant plume dilution.

3.4. Chemical composition and Fe oxidation state of non-buoyant plume particles

Particles sampled from 4089 m depth in the non-buoyant plume were comprised of numerous metallic minerals, a large amount of biological detritus and barite, which could be of hydrothermal or detrital origin (Supplementary information, Table S2). The presence of FeS_2 and another type of Fe-rich particle was determined by SEM-EDX. Large, ~10 μm, FeS_2 particles were aggregates composed of smaller particles < 2 μm (Fig. 6B).

Another type of Fe-rich particle was confirmed to be Fe oxyhydroxides by X-ray absorption spectra (XAS), which showed an absorption profile similar to published spectra for Fe oxyhydroxide minerals, such as ferrihydrite and lepidocrocite (Fig. 7). The spectra for Fe-rich regions of BVF particles revealed that along with Fe sulphide and Fe oxyhydroxide minerals, there were areas where Fe(II) was the predominant oxidation state (*i.e.* Fe(II)-rich mix, Fig. 7).

The XRF map shows two areas of the non-buoyant plume particles enriched in C that coincided with the locations of Fe (circled areas, Fig. 8). In these areas, the C appeared to form a halo around the regions that were also enriched in Fe and O. However, it is possible that this pattern is produced from an element that wasn't detected blocking the C signal in the centre of these regions. Never the less it is clear from these

maps that there is an association amongst Fe, C and O in the imaged particles.

4. Discussion

4.1. Colloid aggregation and particulate Fe during plume dilution

Dilution appears to be the primary factor controlling pFe concentrations, which is consistent with recent inferences from optical sensors in the BVF plume (Estapa et al., 2015). The size range of Fe bearing particles analysed in the plume by SEM-EDX was in the range of 1 to 20 μm, similar to optical sensor determinations made *in situ* by Estapa et al. (2015). These similarities suggest that few significant particle aggregation artefacts could have been caused by our *in-situ* filtration or *ex situ* handling protocols.

The distribution of pFe data relative to conservative mixing in the buoyant plume and the difference between the TDFe/dMn ratio of the end member vent fluid (11.0) and the most vent proximal plume sample (3.3) (Fig. 5B) is consistent with the formation and partial loss of FeS_2, FeS, $CuFeS_2$ and Fe oxyhydroxide particles, during plume dispersion (Lough et al., 2017). Based on the vent fluid Fe/H_2S rapid precipitation of Fe sulphides could account for 32 to 63% of the initial (70 ± 8) Fe precipitation depending on weather Fe precipitates predominantly as FeS or FeS_2. However, loss of this Fe from settling is inconsistent with the TDFe/dMn of the nonbuoyant plume (11.8). We therefore suggest that despite the difference between the vent fluid and buoyant plume TDFe/dMn ratios the vast majority of Fe and Mn must be transported to non-buoyant plume height. This is likely the result of re-entrainment of plume waters around the turbulent margins of the buoyant plume which may not have been captured by our high temperature, low Eh samples from the core of the buoyant plume.

The distribution of buoyant plume pFe relative to the mixing curve in this sample set is in-between that observed previously in buoyant hydrothermal plumes over the MAR (James and Elderfield, 1996) which show particle loss and samples over the East Pacific Rise (EPR) which shows particles behave conservatively (Field and Sherrell, 2000). The similarity between BVF and MAR plume pFe profiles is unsurprising given that deep waters at this site are altered NADW, therefore Fe(II) oxidation rates are similar to those over the MAR (Supplementary information, Table S1) and Fe(II) oxidation is thought to be the rate determining step for Fe oxyhydroxide formation and settling (Field and Sherrell, 2000).

The distribution of pFe in the buoyant plume is easily explained largely by conservative mixing, however, we still need to explain why cFe concentrations rise above the conservative cFe mixing line (Fig. 5B). Assuming there is minimal addition of purely colloidal Fe to the plume at this stage from re-entrainment of plume waters, the increase in cFe can be explained by addition of Fe from either sFe or pFe pools. It is unlikely that any sFe is transformed into cFe as the sFe in the buoyant plume appears to behave conservatively. Instead we propose that, along with pFe losses from gravitational settling, a fraction of pFe in the buoyant plume must add to cFe pool. This could be due to the dissolution or break up of larger particles (Feely et al., 1987) or evidence of a 'microbial Fe pump' (Li et al., 2014) at work in the buoyant plume, where microbes utilize Fe from mineral particles and the eventual cell lysis of those microbes releases Fe colloids. However, the break-up and dissolution of particles may be the best explanation given the short residence time of the buoyant plume which should limit the impact of microbial processes. Based on the difference between pFe and cFe concentrations in the buoyant plume relative to their respective conservative mixing lines the generation of cFe accounts for 3 to 9% of pFe losses during buoyant plume rise relative to the pFe content of the buoyant plume. Alternatively, the increase in cFe could be the result of entraining waters low in pFe and sFe but enriched in cFe at this stage of plume rise potentially from diffuse sources.

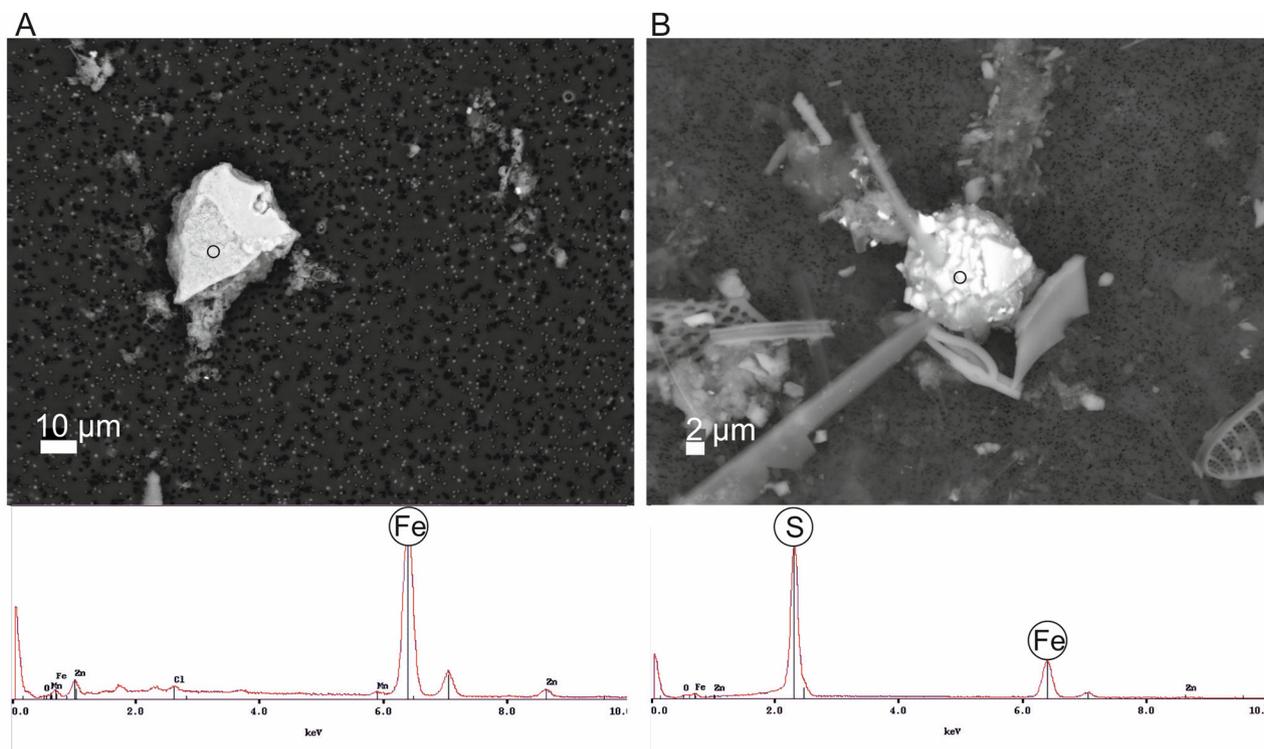We observed an increase in pFe during non-buoyant plume dispersal

Fig. 6. SEM-EDX image of an Fe enriched S depleted particle which is assumed to be an Fe oxyhydroxide (A) from the Fe peak in EDX spectra and a FeS$_2$ aggregate image and spectra (B). Circles show points of EDX analysis.
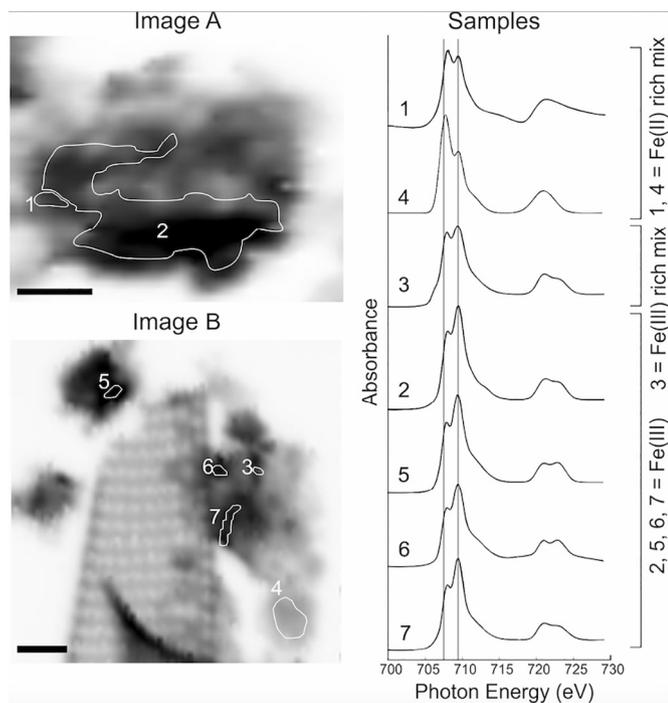

Fig. 7. Iron XAS spectra from Fe-rich regions of BVF non-buoyant plume particles showing Fe oxidation state. STXM absorption images of samples shows Fe-rich areas of interest (1–7). Spectra are classified as in von der Heyden et al. (2012) where spectra can be either pure Fe II, pure Fe III or somewhere in between. Fe sulphide minerals can be classified separately as they do not show the same split peak as Fe oxides. Black scale bars represent 1 μm.

(Fig. 9) consistent with observations from a non-buoyant plume over the EPR (Field and Sherrell, 2000). Furthermore, the increase in pFe over the EPR also coincided with a decrease in the proportion of dFe

relative to TDFe in the plume. This is not immediately apparent when examining our TDFe and dFe data, however when we split dFe further into cFe and sFe a proportional exchange between cFe and pFe is clear (Fig. 9). Field and Sherrell (2000) hypothesised that pFe had been formed by the aggregation of colloidal Fe oxyhydroxides in the dFe fraction. The presence of Fe oxyhydroxide colloids in the EPR plume has since been further evidenced by recent isotope analysis of additional plume samples (Fitzsimmons et al., 2017a). Consistent with this theory of colloidal aggregation, the increase in pFe in the BVF plume coincides with a decrease in cFe (Fig. 9). As a percentage of the TDFe, pFe in the non-buoyant plume increases by 26% with a concomitant decrease in cFe of 22% (Fig. 9). SEM images (Fig. 6A) confirmed larger 10–30 μm particles are aggregates composed of smaller particles, and synchrotron XAS spectra confirm the presence of Fe oxyhydroxides (Fig. 7). This is further supported by re-sampling of a niskin bottle over time which showed a decrease in dFe relative to dMn (Fig. S3). Altogether, our observations strengthen the ideas proposed by Field and Sherrell (2000) that vent derived Fe(II) is oxidised to Fe(III) and forms colloidal Fe oxyhydroxides, which aggregate in the non-buoyant plume to form particulate Fe oxyhydroxides. Colloid aggregation is therefore likely to be a key process in converting dFe to pFe and ultimately limiting the hydrothermal Fe flux to the ocean by removing Fe to sediments. However, from our concentration data alone we cannot determine how much of the observed transfer of cFe to pFe is the result of aggregation between colloidal Fe-oxyhydroxides or other forms of iron colloids aggregating with POC.

Examining the percentage change in cFe and pFe relative to TDFe (Fig. 9) the 22% decrease in cFe would appear to be almost balanced by the 26% increase in pFe, however, as this change occurs with decreasing dMn but relatively constant TDFe then a portion of the decrease in cFe is could be a consequence of plume dilution. This means that on-going colloid aggregation may not fully explain the observed increase in pFe and there are three other factors that may contribute. The first being that there may be an additional source of pFe to the plume that does not add a proportional amount of dMn, sFe, cFe. This
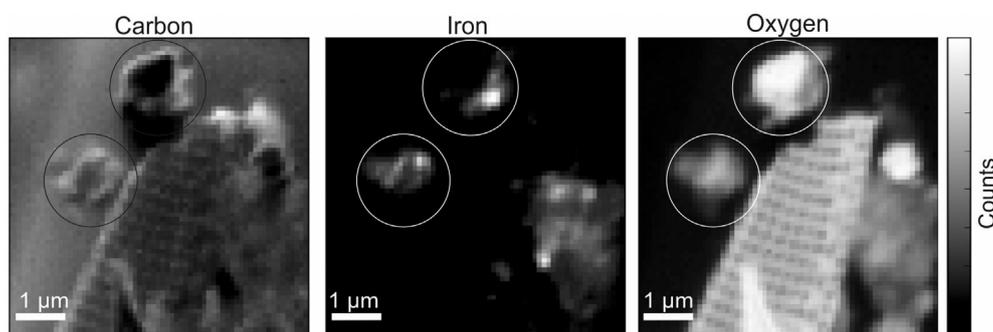
Fig. 8. Synchrotron XRF maps of the same sample shown in Fig. 7, image B for Fe, O, and C. Circled areas indicate where clear overlap in regions enriched in C, Fe and O exist. In the circled regions C enrichment appears to form a halo around the regions enriched in Fe and O. The grey scale indicates intensity of the XRF signal for each element.
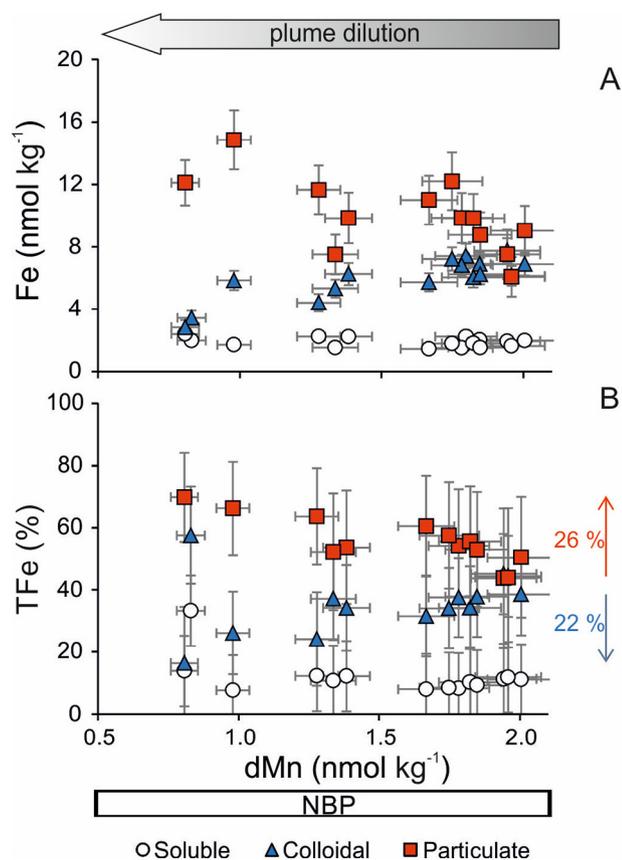
equate to precipitation of 63 ± 12% ($n = 16$) of the dMn from the non-buoyant plume on average, whereas we measure an average non-buoyant plume pMn of 21 ± 14% ($n = 16$). Whilst some precipitation of dMn is inevitable the amount of pMn measured in the non-buoyant plume samples would need to be significantly higher to explain our excess of pFe (and hence TDFe) in the non-buoyant plume. The third factor could be that particles in the non-buoyant plume separate out into layers (independent of the dissolved fraction) as a result of differences in density and size (*i.e.* particle diffusive convection) as demonstrated by Carazzo et al. (2013). This experiment used 300 μm particles with a density of 2.6 g cm^{-3} which are larger than the range we observe of 1 to 20 μm most of which are Fe oxyhydroxides so will have a density similar to ferrihydrite of 3.8 g cm^{-3}. Given the size and density difference between our findings and the experiment of Carazzo et al. (2013) it is unlikely that particle diffusive convection will significantly alter the distribution of pFe to explain our pFe excess in the non-buoyant plume. We therefore conclude that the most likely explanation for additional pFe in the non-buoyant plume is from older waters (either accumulating along an isopycnal within the trench or entrained from beneath the plume) where Fe colloids have aggregated to form pFe and dMn has precipitated. Without further information we are unable to separate the extent to which ongoing colloid aggregation at the time of sampling and addition of pFe rich dMn poor waters contribute to the excess of pFe observed in the non-buoyant plume.

The overlap between the XRF maps of C, Fe and O of particles suggests that particulate organic C may be mixed with Fe oxyhydroxides either by aggregation or adsorption potentially altering the chemical behavior of the Fe oxyhydroxides (Fig. 8) (Aiken et al., 2011). However, it is unclear as to whether this association may facilitate colloid aggregation or buffer against it, or whether it is the result of some other process such as surface adsorption or microbial uptake. The presence of Fe(II) rich regions (Fig. 7) in particles exposed to oxygenated seawater for hours suggests that organic C may stabilize Fe(II), if this also occurs on a colloidal scale the process of colloidal Fe oxyhydroxide formation and subsequent aggregation could be inhibited. This would be consistent with previous work examining particles in sediment traps underneath EPR plume and particles sampled from the non-buoyant plume where regions enriched in Fe(II) were co-located with C regions (Breier et al., 2012; Fitzsimmons et al., 2017b; Hoffman et al., 2018; Toner et al., 2009a). Thus our results add to the growing body of evidence demonstrating that organic C is intimately associated with Fe oxyhydroxides, and organic C may help to create localized regions of Fe(II) enrichment in particles (Bertram et al., 2002; Breier et al., 2012; Toner et al., 2009a). Alternatively, it may be that Fe(II) rich regions represent pyrite that's begun to oxidise and is therefore a mix of Fe(II) and Fe(III). However, we deem this to be a far-less likely explanation given the precautions taken to avoid sample oxidation and the comparatively slow oxidation rates of FeS$_2$ (Gartman and Luther, 2014; Yucel et al., 2011).

Fig. 9. Panel A shows the concentration of Fe in different size fractions of the BVF non-buoyant plume samples. Panel B shows size fractions as a percentage of TDFe. Arrows illustrate the observed change in pFe and cFe with plume dilution in this section of the plume. Vertical error bars in panel B are calculated from the error propagation of errors for TDFe, pFe, cFe and sFe.

could occur if waters where greater precipitation and colloid aggregation of dMn and dFe has occurred and are mixed into the non-buoyant plume. These waters could be entrained from beneath the non-buoyant plume, re-entraining settling Fe particles or could be the result of mixing in of aged plume waters containing suspended pFe that is stored in the water column of the trench at a similar isopycnal to the non-buoyant plume. The homogeneity of density, salinity and potential temperature within the Cayman trench (Connelly et al., 2012) prevents an estimate of the extent to which deep waters from beneath the plume are entrained into the non-buoyant plume (Fig. S2). Secondly if a significant amount of dMn has precipitated in the non-buoyant plume relative to dFe this would make it an unsuitable tracer at this stage of mixing. To explain the TDFe results from the non-buoyant plume in this context an increase in dMn concentrations of 2 to 6 fold is required for TDFe results to lie on the conservative mixing line (Fig. 5A). This would

4.2. Stabilization of Fe in the dissolved fraction

The percentage of dFe composed of cFe in the BVF plume (74 ± 11% cFe) within 1.2 km of the vent source is similar to plumes in the Pacific sampled ~100 km from the EPR (dFe = 76% cFe) (Fitzsimmons et al., 2014) and lower than plumes over the MAR sampled ~500 km from TAG (82 to 96% cFe) (Fitzsimmons et al., 2015b). The similarity between our results proximal to the vent source and more distal studies, suggests a significant fraction of cFe present within 2 km of a hydrothermal source is likely to be transported 1000's of km's into the deep ocean.

It is important to determine the speciation of cFe and sFe during plume dispersion to understand the processes responsible for stabilizing dFe which inhibit complete particle formation of all dFe in the plume. Recent studies suggest cFe and sFe are composed of inorganic colloids (FeS$_2$ or Fe oxyhydroxides) (Fitzsimmons et al., 2017a; Gartman et al., 2014; Yucel et al., 2011), organic Fe complexes (Bennett et al., 2008; Hawkes et al., 2013; Kleint et al., 2016) and/or other Fe(II) species (Sedwick et al., 2015). We consider each of these processes in turn, to reason, which, if any, may account for the stabilization of dFe within the BVF plume.

Pyrite (FeS$_2$) colloids can range from 4 to 200 nm in size (Gartman et al., 2014; Gartman and Luther, 2013, 2014; Yucel et al., 2011), so are small enough to pass through both types of filters used in this study and appear in either sFe or cFe fractions. Colloidal FeS$_2$ is formed instantaneously as vent fluid mixes with seawater and, due to the kinetic stability of these particles over 10s of days, could remain in the dissolved fraction contributing to a significant proportion of dFe export from hydrothermal plumes (Findlay et al., 2015; Gartman et al., 2014; Yucel et al., 2011). This theory is consistent with the dilution profiles of cFe, where the cFe enrichments relative to conservative mixing in early buoyant plume samples could be attributed to colloidal FeS$_2$ formation (Fig. 5B) by the breakdown of larger aggregates (Figs. 6 and 10).

The presence of inorganic Fe oxyhydroxide colloids has been suggested previously (Feely et al., 1996; Field and Sherrell, 2000; Fitzsimmons et al., 2017a) and the pFe data and presence of Fe oxyhydroxide particles discussed in the previous section supports this. Given the stoichiometric excess of Fe in vent fluids from this site relative to H$_2$S (average Fe/H$_2$S = 1.6, n = 7) and the rapid Fe(II) oxidation half-life of 0.28 h (Supplementary information, Table S1), Fe oxyhydroxides are likely to be an additional and predominant source of cFe in the dissolved fraction compared to FeS$_2$. Similarly we would expect this of other vents hosted in ultramafic geology such as Rainbow on the MAR where Fe/H$_2$S is > 1 (Severmann et al., 2004). It is also possible that a fraction of sFe consists of Fe oxyhydroxides which can be as small as 0.002 μm (Baumgartner and Faivre, 2015) however, this maybe an unlikely scenario given the quasi-conservative profile of sFe and the highly reactive nature of Fe oxyhydroxides, assuming that the behavior of Fe oxyhydroxides < 0.02 μm is similar to larger particles > 0.2 μm.

Organic ligands, which form Fe complexes, are small enough to be present in the soluble and colloidal fractions (Cullen et al., 2006; Fitzsimmons et al., 2015a) acting as individual organic carbon molecules that chelate iron or larger colloid sized particles that form surface complexes with Fe. The only study to examine separation of soluble and colloidal organic ligands shows that Fe ligand complexes are predominantly in the soluble pool in the deep ocean (Cullen et al., 2006). In the surface ocean, transition metal ligand complexation is a mechanism by which micro-organisms obtain Fe (Barbeau et al., 2001; Coale and Bruland, 1990). Metal ligand complexation in the surface ocean is, therefore, dependent on the biological demand for these metals and there is a defined pathway for metal complexation and biological uptake. The demand for metals by micro-organisms in hydrothermal plumes and the deep ocean is less clear (Li et al., 2014) and ligands in the deep ocean could come from a number of different sources. Vent-derived Fe could be complexed in the early plume by organic ligands entrained from adjacent diffuse areas (Hawkes et al., 2013; Kleint et al., 2016), organic ligands entrained from deep ocean waters (Bennett et al., 2008), organic ligands formed by abiotic processes during venting (Hawkes et al., 2015) or by sulphide ligands (Gartman et al., 2014; Yucel et al., 2011).

The BVF vent fluids have dissolved organic carbon (DOC) concentrations that are substantially higher than background seawater (BVF = 132 μM compared to 35 to 48 μM in seawater) (Hawkes et al., 2015). Therefore, it is possible that Fe binding organic ligands could be sourced from the vents themselves or from surrounding areas of diffuse flow. If either scenario were significant at BVF, a linear-conservative plume dilution profile would be expected for ligand stabilized Fe species relative to dMn within the plume. A near conservative profile was only observed for sFe in the buoyant plume (Fig. 5) suggesting another possible explanation for the stability of sFe at this site other than FeS$_2$ < 0.02 μm. Furthermore the relatively constant sFe concentration throughout non-buoyant plume dilution (*i.e.* decreasing dMn) (Fig. 9) could be evidence that a baseline sFe pool is maintained by ligand mediated exchange with pFe (Fig. 10) as suggested previously (Fitzsimmons et al., 2017a).
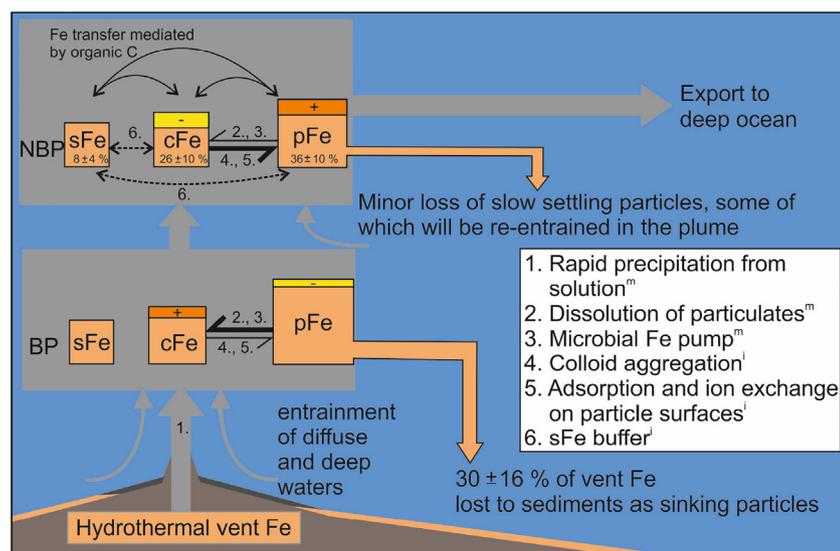
Fig. 10. Summary diagram showing the separation of hydrothermal Fe at different stages of the Beebe plume development as calculated from Eq. (1) and discussed in Sections 4.2 and 4.3. Black arrows between boxes represent transfer of Fe between size fractions, with the wider arrows indicating predominant direction of transfer. The numbers relate to the processes acting to transfer Fe between different fractions given in the white box. The superscript letter i refers to biological and chemical processes "inferred" from our concentration and particle data. Superscript m refers to processes "measured" directly in other studies referenced within the text that we also use to explain changes in Fe concentration. Physical processes such as dispersion (grey) and settling (orange) are implied by arrows.

4.3. Export of dFe from hydrothermal plumes to the deep ocean

Data presented herein shows that a significant portion of vent derived Fe is present in the plume as colloidal and apparently quasi conservative soluble species, which could be dispersed more widely in the deep ocean. To assess the significance of this Fe in the context of the deep ocean Fe inventory, we calculate the mean fraction of vent fluid Fe added to the overlying non-buoyant plume ($f_{xFe/TDFe}$) as sFe and cFe using Eq. (1) and a mean flux of stable Fe species from hydrothermal vents to the deep ocean using Eq. (2).

$$f_{xFe/TDFe} = \sum_n \left(\frac{xFe - swFe}{TDFe} \times \frac{dMn}{TDMn} \right)/n, \tag{1}$$

A mean value for $f_{xFe/TDFe}$ is derived from Eq. (1), where the concentrations of either sFe, cFe or dFe (xFe) and TDFe were determined from n samples in the non-buoyant plume. We assume that TDFe is representative of the diluted vent fluid minus any particulate Fe lost from gravitational settling (Fig. 10). Thus, this does not take into consideration the difference between the vent fluid TDFe/dMn ratio (11.0) compared to the early buoyant plume (3.3) as we think this early buoyant plume sampling may not be entirely representative of the transfer of Fe and Mn to the non-buoyant plume given that the average TDFe/dMn of the non-buoyant plume is similar to the vent fluid (11.8). To be conservative in our calculations, a background seawater correction ($swFe$) is applied to xFe, representative of N. Atlantic waters entering the Cayman Trench (dFe = 0.75 nmol kg^{-1}, sFe = 0.32 nmol kg^{-1}), and multiplied by the dMn to TDMn ratio, similar to Hawkes et al. (2013) to account for the possible entrainment of older recycled plume waters where dMn/TDMn < 1 (dMn/TDMn = 0.8 ± 0.1, $n = 14$, this study). Using this method, the mean vent Fe added to non-buoyant plume was calculated to be 8 ± 4% sFe and 26 ± 10% cFe, giving a combined total of 34 ± 13% dFe with cFe making up the vast majority (Fig. 10). Using the same method, we estimate that 36 ± 10% of vent fluid Fe is transferred to the non-buoyant plume as pFe (Fig. 10). The deficit in this budget suggests that 30 ± 16% of the vent Fe is ultimately lost to sediments as settling of particles within a 1–2 km distance of the vent site.

$$F_{xFe} = f_{xFe/TDFe} \cdot vFe \cdot F_V, \tag{2}$$

An extrapolation to a global flux of dFe from hydrothermal vents was also made using Eq. (2) where the flux (F_{xFe}, mol yr^{-1}) is a product of the fraction of dFe species ($f_{xFe/TDFe}$) in the non-buoyant plume, the volume flux (F_V) and end member hydrothermal Fe concentration (vFe) represented by a global mean value. The global volume flux of seawater passing through high temperature vents has been calculated from chemical and isotopic mass balance of thalium as 7.2×10^{12} kg yr^{-1} (Nielsen et al., 2006), and the global average hydrothermal end-member contains 2.5 mM ($n = 157$, range = 0.8 to 24 mM) (Beaulieu et al., 2013; Bennett et al., 2008; Douville et al., 2002; Elderfield and Schultz, 1996) according to vent fluid data presently available in the InterRidge data base (Beaulieu et al., 2013).

The global flux of dFe estimated from BVF data is 6×10^9 mol yr^{-1} (Table 1). This value is similar to a recent estimate based on high-resolution ocean basin-scale δ^3He:dFe ratios, of 4×10^9 mol yr^{-1} (Resing et al., 2015), but is higher than extrapolated predictions from previous vent-proximal studies (Bennett et al., 2008; Gartman et al., 2014; Hawkes et al., 2013). On the one hand, we cannot assume that the dynamics of any single hydrothermal plume offer an accurate representation of hydrothermal plumes globally. On the other hand, our global flux estimates derived from E2 and Red Lion were based on studies that specifically measured ligand complexation (Bennett et al., 2008; Hawkes et al., 2013), whereas the flux estimates derived from vents on the MAR, EPR and Lau Basin (LA) were calculated from the amount of colloidal FeS$_2$ in plume samples. Therefore, where a specific organic or inorganic stabilization mechanism has been relied upon to

Table 1
Estimating global dissolved Fe fluxes from plume mass balance

	Fe Flux (mol yr^{-1})						
	Near Vent study				Open Ocean Study		
Ridge	MCSC	ESR[a]	MAR[b]	MAR, EPR, LB[c]	EPR[d]	EPR[e]	Model[f]
Vent field	BVF	E2	Red Lion				
Global dFe	6×10^9	1×10^9	7×10^8	9×10^8	7×10^8	4×10^9	9×10^8

a, b and c fluxes are calculated by plume mass balance based on stabilization of 8, 4 and 5% dFe respectively as stated in

[a] Hawkes et al. (2013)
[b] Bennett et al. (2008)
[c] Gartman et al. (2014). Estimate from d, e and f are from
[d] Fitzsimmons et al. (2014)
[e] Resing et al. (2015)
[f] Tagliabue et al. (2010) based on δ^3He:dFe ratios.

determine a dFe flux, it is not surprising that global extrapolations are lower than both Resing et al. (2015) and our findings from the BVF. We take account of the combined influences of organic ligand and inorganic colloid chemistry in our approach, which is consistent with evidence for these combined dFe-stabilization effects described herein and presented elsewhere (Fitzsimmons et al., 2017a; Homoky, 2017).

The similarity between our calculated global dFe fluxes based on the BVF plume and those calculated for the EPR (Resing et al., 2015) using samples up to 4300 km from the EPR vent site, suggests that the majority of plume-derived dFe within several km's of a vent site may eventually be transported thousands of kilometres in the deep ocean. It also emphasizes the critical nature of processes within a few kilometres of the vent field, which seemingly determine the amount of dFe supplied to the deep ocean.

5. Conclusions

Our analysis of Fe concentrations throughout the BVF hydrothermal plume finds that additional pFe is most likely formed by colloid aggregation in the non-buoyant plume. Soluble Fe shows quasi-conservative concentration profiles which means it is a more chemically stable pool of Fe and therefore has the most potential for long distance transport into the deep ocean. Colloid aggregation is understood to be an intermediate step between Fe(II) oxidation and particulate Fe oxyhydroxide formation, and the rate at which this occurs is found to be intimately linked to reactions between Fe, O$_2$ and organic carbon. If BVF is representative of other "black smoker-type plumes", then the global dFe flux from hydrothermal vents will be largely impacted by processes of colloidal aggregation and surface exchange on particles, which are mediated by organic carbon to an unknown degree. The relatively invariant fraction of sFe also indicates that any variability in the flux of dFe from different hydrothermal plumes may also be due to changes in the nature and/or size of the ligand complexed sFe pool. By encompassing the influences of both sFe and cFe processes, we predict dFe fluxes from hydrothermal vents at the upper limit of dFe flux estimates from previous workers. It is therefore vital to further constrain these processes to incorporate them into current modelling techniques that determine the controls on both soluble and colloidal Fe to more accurately simulate dFe in global ocean models, which for example, determine dFe fluxes based on conservative hydrothermal tracers, such as δ^3He.

Appendix A. Supplementary data

Supplementary information is available including sample data, data used for calculating Fe(II) oxidation half-lives and figures showing the LSS, potential temperature and Eh observed during the tow-yo as a cross section. Further details of sampling methods and SEM-EDX are also included. Data files can be obtained from https://www.researchgate.net/profile/Alastair_Lough and https://www.bodc.ac.uk/. Supplementary data to this article can be found online at https://doi.org/10.1016/j.chemgeo.2019.01.001.

References

Aiken, G.R., Hsu-Kim, H., Ryan, J.N., 2011. Influence of dissolved organic matter on the environmental fate of metals, nanoparticles, and colloids. Environ. Sci. Technol. 45 (8), 3196–3201.

Aquilina, A., Homoky, W.B., Hawkes, J.A., Lyons, T.W., Mills, R.A., 2014. Hydrothermal sediments are a source of water column Fe and Mn in the Bransfield Strait, Antarctica. Geochim. Cosmochim. Acta 137 (0), 64–80.

Barbeau, K., Rue, E.L., Bruland, K.W., Butler, A., 2001. Photochemical cycling of iron in the surface ocean mediated by microbial iron(III)-binding ligands. Nature 413 (6854), 409–413.

Baumgartner, J., Faivre, D., 2015. Iron solubility, colloids and their impact on iron (oxyhydr)oxide formation from solution. Earth Sci. Rev. 150, 520–530.

Beaulieu, S.E., Baker, E.T., German, C.R., Maffei, A., 2013. An authoritative global database for active submarine hydrothermal vent fields. Geochem. Geophys. Geosyst. 14 (11), 4892–4905.

Bennett, S.A., et al., 2008. The distribution and stabilisation of dissolved Fe in deep-sea hydrothermal plumes. Earth Planet. Sci. Lett. 270 (3–4), 157–167.

Bennett, S.A., et al., 2011. Dissolved and particulate organic carbon in hydrothermal plumes from the East Pacific Rise, 9 degrees 50′ N. Deep-Sea Res. I Oceanogr. Res. Pap. 58 (9), 922–931.

Bennett, S.A., et al., 2013. Trophic regions of a hydrothermal plume dispersing away from an ultramafic-hosted vent-system: Von Damm vent-site, Mid-Cayman Rise. Geochem. Geophys. Geosyst. 14 (2), 317–327.

Berg, J.C., 2010. An Introduction to Interfaces & Colloids: The Bridge to Nanoscience. World Scientific. http://www.worldscibooks.com/nanosci/7579.html (804 pp.).

Bertram, M.A., Cowen, J.P., Thomson, R.E., Feely, R.A., 2002. Compositional variability in the ascending fluxes from a hydrothermal plume. J. Geophys. Res. Oceans 107 (C11), 12-1–12-13.

Biller, D.V., Bruland, K.W., 2012. Analysis of Mn, Fe, Co, Ni, Cu, Zn, Cd, and Pb in seawater using the Nobias-chelate PA1 resin and magnetic sector inductively coupled plasma mass spectrometry (ICP-MS). Mar. Chem. 130, 12–20.

Bischoff, J.L., Dickson, F.W., 1975. Seawater basalt interactions at 200 degrees C and 500 bars - implications for the origin of seafloor heavy metal deposits and regulation of seawater chemistry. Earth Planet. Sci. Lett. 25 (3), 385–397.

Bischoff, J.L., Seyfried, W.E., 1978. Hydrothermal chemistry of seawater from 25 degrees C to 350 degrees C. Am. J. Sci. 278 (6), 838–860.

Boye, M., et al., 2010. Significant portion of dissolved organic Fe complexes in fact is Fe colloids. Mar. Chem. 122 (1–4), 20–27.

Breier, J.A., et al., 2012. Sulfur, sulfides, oxides and organic matter aggregated in submarine hydrothermal plumes at 9 degrees 50′ N East Pacific Rise. Geochim. Cosmochim. Acta 88, 216–236.

Carazzo, G., Jellinek, A.M., Turchyn, A.V., 2013. The remarkable longevity of submarine plumes: Implications for the hydrothermal input of iron to the deep-ocean. Earth Planet. Sci. Lett. 382, 66–76.

Coale, K.H., Bruland, K.W., 1990. Spatial and temporal variability in copper complexation in the North Pacific. Deep Sea Res. Part A 37 (2), 317–336.

Connelly, D.P., et al., 2012. Hydrothermal vent fields and chemosynthetic biota on the world's deepest seafloor spreading centre. Nat. Commun. 3, 620.

Cowen, J.P., Massoth, G.J., Baker, E.T., 1986. Bacterial scavenging of Mn and Fe in a Mid Field to Far Field hydrothermal particle plume. Nature 322 (6075), 169–171.

Cowen, J.P., Massoth, G.J., Feely, R.A., 1990. Scavenging rates of dissolved manganese in a hydrothermal vent plume. Deep Sea Res. Part A 37 (10), 1619–1637.

Cowen, J.P., et al., 2001. Ascending and descending particle flux from hydrothermal plumes at Endeavour Segment, Juan de Fuca Ridge. Deep-Sea Res. I Oceanogr. Res. Pap. 48 (4), 1093–1120.

Cullen, J.T., Bergquist, B.A., Moffett, J.W., 2006. Thermodynamic characterization of the partitioning of iron between soluble and colloidal species in the Atlantic Ocean. Mar.

Chem. 98 (2–4), 295–303.

de Groot, F.M.F., 2009. XANES spectra of transition metal compounds. J. Phys. Conf. Ser. 190 (1), 012004.

Douville, E., et al., 2002. The rainbow vent fluids (36 degrees 14′ N, MAR): the influence of ultramafic rocks and phase separation on trace metal content in Mid-Atlantic Ridge hydrothermal fluids. Chem. Geol. 184 (1–2), 37–48.

Edmond, J.M., et al., 1979. Ridge crest hydrothermal activity and the balances of the major and minor elements in the ocean - Galapagos data. Earth Planet. Sci. Lett. 46 (1), 1–18.

Edmonds, H.N., German, C.R., 2004. Particle geochemistry in the Rainbow hydrothermal plume, Mid-Atlantic Ridge. Geochim. Cosmochim. Acta 68 (4), 759–772.

Elderfield, H., Schultz, A., 1996. Mid-ocean ridge hydrothermal fluxes and chemical composition of the ocean. Annu. Rev. Earth Planet. Sci. 24, 191–224.

Estapa, M.L., Breier, J.A., German, C.R., 2015. Particle dynamics in the rising plume at Piccard Hydrothermal Field, Mid-Cayman Rise. Geochem. Geophys. Geosyst. 16 (8), 2762–2774.

Feely, R.A., et al., 1987. Composition and dissolution of black smoker particulates from active vents on the Juan de Fuca ridge. J. Geophys. Res. Solid Earth Planets 92 (B11), 11347–11363.

Feely, R.A., Gendron, J.F., Baker, E.T., Lebon, G.T., 1994a. Hydrothermal plumes along the east pacific rise, 8-degrees-40′ to 11-degrees-50′N - particle distribution and composition. Earth Planet. Sci. Lett. 128 (1–2), 19–36.

Feely, R.A., et al., 1994b. Composition and sedimentation of hydrothermal plume particles from North Cleft Segment, Juan De Fuca Ridge. J. Geophys. Res. Solid Earth 99 (B3), 4985–5006.

Feely, R.A., et al., 1996. Hydrothermal plume particles and dissolved phosphate over the superfast-spreading southern East Pacific Rise. Geochim. Cosmochim. Acta 60 (13), 2297–2323.

Feely, R.A., Trefry, J.H., Lebon, G.T., German, C.R., 1998. The relationship between P/Fe and V/Fe ratios in hydrothermal precipitates and dissolved phosphate in seawater. Geophys. Res. Lett. 25 (13), 2253–2256.

Field, M.P., Sherrell, R.M., 2000. Dissolved and particulate Fe in a hydrothermal plume at 9 degrees 45′ N, East Pacific Rise: slow Fe (II) oxidation kinetics in Pacific plumes. Geochim. Cosmochim. Acta 64 (4), 619–628.

Findlay, A.J., Gartman, A., Shaw, T.J., Luther, G.W., 2015. Trace metal concentration and partitioning in the first 1.5 m of hydrothermal vent plumes along the Mid-Atlantic Ridge: TAG, Snakepit, and Rainbow. Chem. Geol. 412, 117–131.

Fitzsimmons, J.N., Boyle, E.A., Jenkins, W.J., 2014. Distal transport of dissolved hydrothermal iron in the deep South Pacific Ocean. Proc. Natl. Acad. Sci. U. S. A. 111 (47), 16654–16661.

Fitzsimmons, J.N., Bundy, R.M., Al-Subiai, S.N., Barbeau, K.A., Boyle, E.A., 2015a. The composition of dissolved iron in the dusty surface ocean: an exploration using size-fractionated iron-binding ligands. Mar. Chem. 173, 125–135.

Fitzsimmons, J.N., et al., 2015b. Partitioning of dissolved iron and iron isotopes into soluble and colloidal phases along the GA03 GEOTRACES North Atlantic Transect. Deep-Sea Res. II Top. Stud. Oceanogr. 116, 130–151.

Fitzsimmons, J.N., et al., 2017a. Iron persistence in a distal hydrothermal plume supported by dissolved-particulate exchange. Nat. Geosci. 10 (3), 195–201.

Fitzsimmons, J.N., et al., 2017b. Iron persistence in a distal hydrothermal plume supported by dissolved–particulate exchange. Nat. Geosci. 10, 195.

Gartman, A., Luther, G.W., 2013. Comparison of pyrite (FeS₂) synthesis mechanisms to reproduce natural FeS₂ nanoparticles found at hydrothermal vents. Geochim. Cosmochim. Acta 120, 447–458.

Gartman, A., Luther, G.W., 2014. Oxidation of synthesized sub-micron pyrite (FeS₂) in seawater. Geochim. Cosmochim. Acta 144, 96–108.

Gartman, A., Findlay, A.J., Luther, G.W., 2014. Nanoparticulate pyrite and other nano-particles are a widespread component of hydrothermal vent black smoker emissions. Chem. Geol. 366, 32–41.

German, C., 2016. GEOTRACES Royal Society Meeting on Ocean Boundary Fluxes. (in prep).

German, C., Von Damm, K.L., 2004. Hydrothermal processes. In: Elderfield, H. (Ed.), The Oceans and Marine Geochemistry. Treatise on Geochemistry. Elsevier-Pergamon, Oxford, pp. 182–216.

German, C.R., Campbell, A.C., Edmond, J.M., 1991. Hydrothermal scavenging at the Mid-Atlantic Ridge - modification of trace-element dissolved fluxes. Earth Planet. Sci. Lett. 107 (1), 101–114.

German, C.R., et al., 2010. Diverse styles of submarine venting on the ultraslow spreading Mid-Cayman Rise. Proc. Natl. Acad. Sci. U. S. A. 107 (32), 14020–14025.

Goldstein, J., et al., 2003. Scanning Electron Microscopy and X-ray Microanalysis. Springer, New York.

Hawkes, J.A., Connelly, D.P., Gledhill, M., Achterberg, E.P., 2013. The stabilisation and transportation of dissolved iron from high temperature hydrothermal vent systems. Earth Planet. Sci. Lett. 375, 280–290.

Hawkes, J.A., et al., 2015. Efficient removal of recalcitrant deep-ocean dissolved organic matter during hydrothermal circulation. Nat. Geosci. 8 (11), 856.

Hawkings, J.R., et al., 2014. Ice sheets as a significant source of highly reactive nano-particulate iron to the oceans. Nat. Commun. 5, 8.

Hoffman, C.L., et al., 2018. Near-field iron and carbon chemistry of non-buoyant hydrothermal plume particles, Southern East Pacific Rise 15°S. Mar. Chem. 201, 183–197.

Homoky, W.B., 2017. Biogeochemistry: deep ocean iron balance. Nat. Geosci. 10 (3), 162–163.

Homoky, W.B., et al., 2011. Iron and manganese diagenesis in deep sea volcanogenic sediments and the origins of pore water colloids. Geochim. Cosmochim. Acta 75 (17), 5032–5048.

Israelachvili, J.N., 2011. The forces between atoms and molecules. In: Intermolecular and

Surface Forces, Third edition. Academic Press, San Diego, pp. 1–18.

James, R.H., Elderfield, H., 1996. Dissolved and particulate trace metals in hydrothermal plumes at the Mid-Atlantic Ridge. Geophys. Res. Lett. 23 (23), 3499–3502.

James, R.H., Elderfield, H., Palmer, M.R., 1995. The chemistry of hydrothermal fluids from the broken spur site, 29 degrees N Mid Atlantic Ridge. Geochim. Cosmochim. Acta 59 (4), 651–659.

James, R.H., et al., 2014. Composition of hydrothermal fluids and mineralogy of associated chimney material on the East Scotia Ridge back-arc spreading centre. Geochim. Cosmochim. Acta 139, 47–71.

Johns, W.E., Townsend, T.L., Fratantoni, D.M., Wilson, W.D., 2002. On the Atlantic inflow to the Caribbean Sea. Deep-Sea Res. I Oceanogr. Res. Pap. 49 (2), 211–243.

Kagaya, S., et al., 2009. A solid phase extraction using a chelate resin immobilizing carboxymethylated pentaethylenehexamine for separation and preconcentration of trace elements in water samples. Talanta 79 (2), 146–152.

Kleint, C., Hawkes, J.A., Sander, S.G., Koschinsky, A., 2016. Voltammetric investigation of hydrothermal iron speciation. Front. Mar. Sci. 3.

Klevenz, V., 2011. Geochemistry of vent fluid particles formed during initial hydrothermal fluid–seawater mixing along the Mid-Atlantic Ridge. Geochem. Geophys. Geosyst. 12.

Lam, P.J., et al., 2017. Size-fractionated distributions of suspended particle concentration and major phase composition from the U.S. GEOTRACES Eastern Pacific Zonal Transect (GP16). Mar. Chem. 201, 90–107.

Lerotic, M., Mak, R., Wirick, S., Meirer, F., Jacobsen, C., 2014. MANTiS: a program for the analysis of X-ray spectromicroscopy data. J. Synchrotron Radiat. 21 (5), 1206–1212.

Li, M., et al., 2014. Microbial iron uptake as a mechanism for dispersing iron from deep-sea hydrothermal vents. Nat. Commun. 5, 8.

Lough, A.J.M., et al., 2017. Opposing authigenic controls on the isotopic signature of dissolved iron in hydrothermal plumes. Geochim. Cosmochim. Acta 202, 1–20.

Martin, J.H., 1990. Glacial-interglacial CO_2 change: the iron hypothesis. Paleoceanography 5 (1), 1–13.

Metz, S.a.T., John, H., 1993. Field and laboratory studies of metal uptake and release by hydrothermal precipitates. J. Geophys. Res. Solid Earth 98 (B6), 2156–2202.

Milne, A., Landing, W., Bizimis, M., Morton, P., 2010. Determination of Mn, Fe, Co, Ni, Cu, Zn, Cd and Pb in seawater using high resolution magnetic sector inductively coupled mass spectrometry (HR-ICP-MS). Anal. Chim. Acta 665 (2), 200–207.

Nielsen, S.G., et al., 2006. Hydrothermal fluid fluxes calculated from the isotopic mass balance of thallium in the ocean crust. Earth Planet. Sci. Lett. 251 (1–2), 120–133.

Nishioka, J., Obata, H., Tsumune, D., 2013. Evidence of an extensive spread of hydrothermal dissolved iron in the Indian Ocean. Earth Planet. Sci. Lett. 361, 26–33.

Resing, J.A., et al., 2015. Basin-scale transport of hydrothermal dissolved metals across the South Pacific Ocean. Nature 523 (7559), 200–U140.

Revels, B.N., Ohnemus, D.C., Lam, P.J., Conway, T.M., John, S.G., 2015. The isotopic signature and distribution of particulate iron in the North Atlantic Ocean. Deep-Sea Res. II Top. Stud. Oceanogr. 116, 321–331.

Russel, W.B., Saville, D.A., Schowalter, W.R., 1989. Colloidal dispersions. In: Cambridge Monographs on Mechanics. Cambridge University Press, Cambridge.

Saito, M.A., et al., 2013. Slow-spreading submarine ridges in the South Atlantic as a significant oceanic iron source. Nat. Geosci. 6 (9), 775–779.

Sander, S.G., Koschinsky, A., 2011. Metal flux from hydrothermal vents increased by organic complexation. Nat. Geosci. 4 (3), 145–150.

Sands, C.M., Connelly, D.P., Statham, P.J., German, C.R., 2012. Size fractionation of trace metals in the Edmond hydrothermal plume, Central Indian Ocean. Earth Planet. Sci. Lett. 319, 15–22.

Sedwick, P.N., Sohst, B.M., Ussher, S.J., Bowie, A.R., 2015. A zonal picture of the water column distribution of dissolved iron(II) during the U.S. GEOTRACES North Atlantic transect cruise (GEOTRACES GA03). Deep-Sea Res. II Top. Stud. Oceanogr. 116, 166–175.

Severmann, S., et al., 2004. The effect of plume processes on the Fe isotope composition of hydrothermally derived Fe in the deep ocean as inferred from the Rainbow vent site, Mid-Atlantic Ridge, 36°14′N. Earth Planet. Sci. Lett. 225 (1–2), 63–76.

Statham, P.J., German, C.R., Connelly, D.P., 2005. Iron(II) distribution and oxidation kinetics in hydrothermal plumes at the Kairei and Edmond vent sites, Indian Ocean. Earth Planet. Sci. Lett. 236 (3–4), 588–596.

Tagliabue, A., et al., 2010. Hydrothermal contribution to the oceanic dissolved iron inventory. Nature 3, 252–256.

Toner, B.M., et al., 2009a. Preservation of iron(II) by carbon-rich matrices in a hydrothermal plume. Nat. Geosci. 2 (3), 197–201.

Toner, B.M., et al., 2009b. Biogenic iron oxyhydroxide formation at mid-ocean ridge hydrothermal vents: Juan de Fuca Ridge. Geochim. Cosmochim. Acta 73 (2), 388–403.

Toner, B.M., German, C.R., Dick, G.J., Breier, J.A., 2016. Deciphering the complex chemistry of deep-ocean particles using complementary synchrotron X-ray microscope and microprobe instruments. Acc. Chem. Res. 49 (1), 128–137.

Von Damm, K.L., Edmond, J.M., Grant, B., Measures, C.I., 1985. Chemistry of submarine hydrothermal solutions at 21-degrees-N, East Pacific Rise. Geochim. Cosmochim. Acta 49 (11), 2197–2220.

von der Heyden, B.P., Roychoudhury, A.N., Mtshali, T.N., Tyliszczak, T., Myneni, S.C.B., 2012. Chemically and geographically distinct solid-phase iron pools in the southern ocean. Science 338 (6111), 1199–1201.

Vondamm, K.L., Bischoff, J.L., 1987. Chemistry of hydrothermal solutions from the Southern Juan de Fuca ridge. J. Geophys. Res. Solid Earth Planets 92 (B11), 11334–11346.

Waeles, M., et al., 2017. On the early fate of hydrothermal iron at deep-sea vents: a reassessment after in situ filtration. Geophys. Res. Lett. 44 (9), 4233–4240.

Webber, A.P., Roberts, S., Murton, B.J., Hodgkinson, M.R.S., 2015. Geology, sulfide geochemistry and supercritical venting at the Beebe Hydrothermal Vent Field, Cayman Trough. Geochem. Geophys. Geosyst. 16 (8), 2661–2678.

Wu, J., Boyle, E., Sunda, W., Wen, L.-S., 2001. Soluble and Colloidal Iron in the Oligotrophic North Atlantic and North Pacific. Science 293 (5531), 847–849.

Yucel, M., Gartman, A., Chan, C.S., Luther, G.W., 2011. Hydrothermal vents as a kinetically stable source of iron-sulphide-bearing nanoparticles to the ocean. Nat. Geosci. 4 (6), 367–371.